Compound Supershear Rupture During the 2026 Venezuela Earthquake Doublet

Ryo Yamaguchi[1,*], Naohiro Inoue[1], Takeshi Saito[2], Hayato Tanaka[2], Nozomi Ishida[1], Bogdan Enescu[3,4], Tuncay Taymaz[5,6], Ryo Okuwaki[7] and Yuji Yagi[7,*]

[1] Graduate School of Science and Technology, University of Tsukuba, Ten'nodai 1-1-1, Tsukuba, 305–8572, Ibaraki, Japan

[2] School of Life and Environmental Sciences, University of Tsukuba, Ten'nodai 1-1-1, Tsukuba, 305-8572, Ibaraki, Japan

[3] Department of Geophysics, Graduate School of Science, Kyoto University, Kitashirakawa, Oiwake-cho, Sakyo-ku, Kyoto 606-8502, Japan

[4] National Institute for Earth Physics, Calugareni str. 12, P.O. Box MG-2, Magurele-Bucharest, Ilfov, 077125, Romania

[5] Department of Geophysical Engineering, The Faculty of Mines, İstanbul Technical University, İTÜ Maslak Campus, Sarıyer 34469, İstanbul, Türkiye

[6] Disaster Management Institute, İstanbul Technical University, İTÜ Maslak Campus, Sarıyer 34469, İstanbul, Türkiye

[7] Institute of Life and Environmental Sciences, University of Tsukuba, Ten'nodai 1-1-1, Tsukuba, 305–8572, Ibaraki, Japan

[*]Corresponding Authors: Ryo Yamaguchi (yama0109@geol.tsukuba.ac.jp) and
Yuji Yagi (yagi-y@geol.tsukuba.ac.jp)

Key Points

- The 2026 Venezuela earthquake doublet ruptured mainly eastward along a complex transform-fault system.
- The rupture reached supershear speeds and exhibited three apparent stalls accompanied by changes in the inferred fault orientation.
- A high-slip-rate subevent behind the leading apparent rupture front may have initiated or resumed eastward supershear propagation.

Abstract

The 24 June 2026 Venezuela earthquake doublet occurred along a complex transform-fault system. Teleseismic P waves encompassing both cataloged events were analyzed using potency density tensor inversion with seven structure models. All models indicate predominantly eastward rupture over approximately 220 km, including several stages of supershear propagation. Three apparent rupture stalls coincided with changes in the inferred fault orientation, suggesting that fault bends or transitions between fault segments may have influenced rupture propagation. A high-slip-rate subevent occurred about 90 km behind the apparent rupture front 37 s after the origin time of the first event. Whether this subevent reflects back-propagating rupture or a relatively independent rupture episode remains unresolved, but rapid eastward rupture appears to have initiated or resumed afterward. This compound rupture process raises the possibility that parts of the source region experienced repeated strong shaking.

Plain Language Summary

On 24 June 2026, an earthquake doublet occurred in northern Venezuela. Its source region lies along a complex fault system where the South American, Caribbean, and North Andes plates mainly slide past one another. We analyzed seismic waves recorded worldwide using a method that estimates slip evolution and fault geometry simultaneously. The results suggest that the rupture propagated mainly eastward for about 220 km, reaching 5–6 km/s during several stages, faster than shear waves travel through the surrounding rocks. The rupture also showed three apparent pauses near locations where the fault orientation changed, suggesting that bends or transitions between fault segments influenced its propagation. About 37 s after the first earthquake began, a strong slip episode occurred roughly 90 km behind the leading rupture front. It remains unclear whether this episode resulted from rupture propagating backward or from a separate rupture episode, but rapid eastward propagation appears to have started or resumed afterward. These multiple episodes of rapid rupture propagation highlight the complexity of the 2026 Venezuela doublet and may have implications for the duration and spatial distribution of strong shaking.

1. Introduction

Strike-slip earthquakes are often reported to have multiplicity of rupture episodes and complexities in rupture speed and direction (e.g., Abdelmeguid et al., 2023; Archuleta, 1984; Bao et al., 2019; Bouchon et al., 2010; Bouin et al., 2004; Dunham & Archuleta, 2004; Jia et al., 2023; Liu et al., 2023; Ren et al., 2024; Vallée et al., 2008), which are attributed, for example, to the heterogeneity of fault strength and geometric complexity of faults (e.g., Hicks et al., 2020; Tadapansawut et al., 2021; Zhou et al., 2025; Zhang et al., 2023). These rupture properties pose challenges to stable and robust modeling of earthquake source processes for finite-fault inversion approaches prescribing a priori fault geometry and rupture properties, and modeling errors arise if the prescribed scenario differs from the true one (Liu et al., 2023; Ragon et al., 2018; Shimizu et al., 2020). These modeling errors become more pronounced particularly in strike-slip earthquakes, for which slight changes in fault geometry impact Green's functions and hence an inverted solution (Shimizu et al., 2020; Yamashita et al., 2021). Therefore, stable analysis of earthquakes in geometrically complex fault systems requires an approach that does not constrain the slip direction to a prescribed fault plane but instead extracts spatiotemporal variations in focal mechanism from the observed data, thereby providing constraints on the fault geometry (e.g., Sato et al., 2026; Shimizu et al., 2021).

On June 24, 2026, a large strike-slip earthquake occurred in northern Venezuela. The U.S. Geological Survey (USGS) reported two right-lateral strike-slip events as a doublet: a moment magnitude (M_W) 7.2 event, followed 32 s later by an M_W 7.5 event (USGS, 2017, 2026a, 2026b). Aftershocks during the first three days were distributed over an approximately 250-km-long region from 66.5°W to 68.5°W (Figure 1a) (FUNVISIS, 2026; USGS, 2017). This distribution suggests predominantly eastward rupture propagation from the initial epicenter, although it remains unclear whether this propagation was associated with the M_W 7.2 event, the M_W 7.5 event, or both. Surface deformation associated with this earthquake inferred from InSAR is also concentrated east of the epicenter (e.g., NASA Earth Observatory, 2026). However, because the northern half of the source region lies offshore, InSAR provides limited constraints on deformation in this area, making it difficult to constrain the detailed fault geometry. The possible source region of the 2026 earthquake sequence is attributed to a transform fault system that forms part of the right-lateral strike-slip boundary accommodating approximately 20 mm/yr of relative plate motion (DeMets et al., 2010) between the South American plate and Caribbean–North Andes plates (Figure 1a; Bird, 2003). Several large earthquakes occurred along this system before the 2026 event (Audemard, 2003, 2007; Audemard et al., 2006, 2025; Colón et al., 2015; Paige, 1930) including the 1812 earthquake, which is inferred to have involved at least two M7-class subevents and was the most destructive earthquake in Venezuelan history (Choy et al., 2010; Dewey, 1972).

Geological surveys and geodetic measurements suggest a slip deficit of 1–4 m, accumulated since 1812 along the eastern part of the Boconó fault (Pousse-Beltran et al., 2017, 2018). Within the source region of the 2026 doublet, the active faults of Boconó and San Sebastián accommodate the plate boundary and exhibit a curved geometry (Figure 1e) (Alvarado et al., 2017; Styron & Pagani, 2020). The two major active faults are bounded by the sub-parallel Puerto Cabello fault, at the eastern end of the Boconó fault. The NW-SE oriented Tacagua–El Ávila fault apparently intersects the eastern section of the San Sebastian fault (Figure 1e) (Alvarado et al., 2017; Audemard et al., 2000; Styron & Pagani, 2020). These features collectively suggest that the 2026 Venezuela earthquake doublet ruptured faults with spatially variable geometry, for which the assumption of a simple planar fault may be inappropriate (see e.g., Liu et al., 2026).

Potency density tensor inversion (PDTI) (Shimizu et al., 2020) has been successfully applied to large earthquakes involving geometrically complex fault systems because it resolves the spatiotemporal evolution of rupture, including changes in focal mechanism, without prescribing a fixed fault geometry (e.g., Inoue et al., 2025; Ohara et al., 2023; Okuwaki et al., 2021, 2023; Yagi et al., 2023; Yamaguchi et al., 2025). Here we apply PDTI to teleseismic P waves of the 2026 Venezuela earthquake doublet to resolve its rupture process and examine how the rupture evolved within the geometrically complex transform fault system and how the two cataloged events are related within the overall rupture sequence.

2. Data and Method

In the PDTI method, fault slip on multiple fault planes is projected onto a model plane and represented as a set of potency density tensors (Shimizu et al., 2020). The potency density tensor is expressed as a linear combination of the five basis double couples proposed by Kikuchi & Kanamori (1991). This representation allows fault geometry and rupture evolution to be estimated simultaneously without prescribing the fault geometry a priori (Shimizu et al., 2020). With this highly flexible PDTI parameterization, the strong non-negativity constraints conventionally used to restrict fault-slip directions to physically plausible ranges cannot, in principle, be imposed. Yagi & Fukahata (2011) developed the first formulation capable of stably resolving detailed rupture processes without such strong constraints by explicitly incorporating modeling errors in teleseismic P-wave Green's functions into the data covariance matrix and jointly determining the variance of the Green's-function errors and the strength of the smoothing constraint through the minimization of Akaike's Bayesian Information Criterion (ABIC; Akaike, 1980; Sato et al., 2022; Yabuki & Matsu'ura, 1992). The PDTI method extends the formulation of Yagi & Fukahata (2011). Although its current implementation is limited to teleseismic P-wave data, for which Green's-function errors can be appropriately formulated, its utility has been demonstrated through applications to a variety of complex earthquakes (Hicks et al., 2020; Okuwaki et al., 2020; Yagi et al., 2023). In this study, we used the time-adaptive smoothing implementation of the PDTI method, which reduces temporal over-smoothing (Yamashita et al., 2022).

We treated the M_W 7.2 and M_W 7.5 events as a series in our inversion procedure given that the two events occurred only 32 s apart (USGS, 2026a, 2026b). We used vertical-component teleseismic P-wave records downloaded from the SAGE Wilber 3 system and obtained at epicentral distances of 30°–90°. We selected 47 stations based on their azimuthal coverage of the source and signal-to-noise ratios that allowed reliable picking of the P-wave arrival times (Figure 1c). The P-wave arrival times were manually picked. The instrument responses were then removed, and the records were converted to velocity waveforms with a sampling interval of 0.5 s. Theoretical Green's functions were calculated at intervals of 0.1 s following Kikuchi & Kanamori (1991), using ray parameters and travel times calculated with the TauP toolkit (Crotwell et al., 1999). To assess the sensitivity of the results to Green's-function errors arising from uncertainty in the structure model, we performed inversions using six 1-D structure models derived from CRUST1.0 (Laske et al., 2013) and one based on ak135-F (Kennett et al., 1995; Montagner & Kennett, 1996) (see Tables S1–S7 in Supporting Information).

The model fault was represented by a vertical, nonplanar surface constructed along the mapped traces of the Boconó and San Sebastián faults (Styron & Pagani, 2020) (Figure 1e). We evaluated the sensitivity of the solution to the assumed fault geometry using an alternative planar fault model and found that the main features of the solution remain unchanged (Figure S5 in Supporting Information). The knot spacing was set at 6 km in both the strike and dip directions. Based on the aftershock distributions determined by the USGS and FUNVISIS, the along-strike length and down-dip width of the model surface were set to 246 km and 24 km, respectively. The initial rupture point was placed on the modeled surface, near the epicentral locations of the M_W 7.2 event independently determined by the USGS and FUNVISIS (Figure 1e), and its depth was fixed at 20 km following the hypocentral depth of the M_W 7.2 event determined by FUNVISIS (2026). The potency-rate density function at each knot was represented by linear B-spline basis functions spaced at 0.5 s intervals over a 48 s time window. The total source duration was set to 80 s to encompass the complete rupture process of the doublet. The velocity of the hypothesized model-space front, V_r, was set to 5 km/s. We note that this boundary does not necessarily correspond to the rupture-front velocity because potency rate can be resolved behind the hypothesized front where required by the data (e.g., Hicks et al., 2020). This flexibility allows the inversion to represent a range of rupture behaviors, including supershear and back-propagating rupture.

We assessed the sensitivity of the solution to this setting using V_r values of 4 and 6 km/s (Figure S6 in Supporting Information). To implement the time-adaptive smoothing constraint (Yamashita et al., 2022), we rotated the set of five basis double couples so that one basis component was aligned with the double-couple mechanism that best matched the GCMT solution (Dziewonski et al., 1981; Ekström et al., 2012). For simplicity, we hereafter refer to potency density and potency-rate density as slip and slip rate, respectively.

3. Results

To assess the robustness of the solution, we applied the PDTI method to the 2026 Venezuela earthquake and performed seven inversions using seven different 1-D structure models. The total moment tensor solution calculated by spatiotemporal integration of the potency-rate density tensor consistently showed a right-lateral strike-slip mechanism in all seven models (Figure 1b). The total seismic moment range was 3.8–4.1×10^{20} N m (M_W 7.7) (Figure S2 in Supporting Information). The slip distribution showed that the rupture propagated over a region extending about 220 km east and about 20 km west of the epicenter in all models (Figures 1e and S2 in Supporting Information). The maximum slip range was 2.9–4.0 m, and the average slip range was 1.4–1.9 m. In all seven models, the moment-rate functions exhibited two major episodes of moment release, spanning 28–40 s and 40–60 s after the origin time of the first event (Figure 1a). Hereafter, all times are given relative to this origin time, defined as 0 s. Synthetic waveforms generated from all seven models reproduced the main features of the observed waveforms well (Figure S1 in the Supporting Information).

In the following presentation and discussion of the results, we focus only on features consistently resolved by all seven models (Figures S2 and S3 in the Supporting Information) and report the median values across the models. To facilitate visualization of the temporal continuity of the fault-plane geometry, strike values are expressed as reduced strikes within the range 0° to 180°. Hereafter, these values are referred to as reduced strikes. The corresponding dips are represented as oriented dips, with values greater than 90° used when the original strikes exceed 180°. The PDTI method resolves the spatiotemporal distribution of slip rate but does not resolve the rupture front directly. For each model, we tracked the leading edge of the region where the slip rate exceeded 40% of the maximum slip rate over the complete modeled spatiotemporal distribution and referred to this edge as the apparent rupture front. This operational definition is used for describing the apparent rupture velocity and direction and is not intended to represent the rupture front itself; as shown below, substantial slip also occurred well behind this edge, which therefore does not capture the full spatiotemporal complexity of the slip-rate distribution. We confirmed that the inferred propagation pattern was insensitive to threshold values between 30 and 50% (Figure S4 in Supporting Information).

After the rupture initiation, the apparent rupture front mainly propagated up-dip and slightly eastward until 4 s (Figure 2b). From 4 to 13 s, the rupture continued propagating eastward at approximately 5 km/s (Figure 1f). This speed exceeds the local S-wave velocity of 3.5–3.7 km/s at depths shallower than 20 km in the source region (Tables S1–S3 in Supporting Information). During 13–18 s, the apparent rupture front stalled around 50 km east of the epicenter (Figure 1f). The reduced strike increased from 80° to 86° between 4 and 13 s and then remained between 85° and 87° until 18 s (Figure 1g). The oriented dip oscillated between 84° and 94° between 4 and 13 s, then exhibited a decreasing trend until 18 s, reaching a minimum value of 81° at 16 s (Figure 1h).

From 18 to 34 s, the apparent rupture front propagated eastward, with a short stall at a location approximately 100 km east of the epicenter, during the 23–26 s time interval (Figure 1f). The average apparent rupture velocity was approximately 5.5–6 km/s (Figure 1f). A similar velocity was obtained using an alternative setting of the model-space boundary (Figure S6). From 34 to 41 s, the apparent rupture front stalled at a location approximately 140–160 km east of the epicenter. Between 18 and 41 s, the reduced strike remained within a narrow range of 85°–90°, while the oriented dip gradually decreased from 83° to 78° (Figures 1g and 1h). During this interval, eastward rupture propagation was interrupted by two apparent stalls.

Eastward rupture propagation resumed at 41 s, from a point approximately 20 km west of the easternmost position reached before the stall (Figure 1f). The rupture then continued to propagate eastward until 56 s at an average velocity of approximately 5 km/s (Figures 1f and 2b). The reduced strike increased from 85° at 41 s to 92° at 46 s, and then decreased to 78° by 57 s. The oriented dip remained nearly constant at approximately 79° until 44 s, increased to approximately 84° by 46 s, and remained within the range of 84°–86° until 53 s. After 53 s, the model-to-model variability increased.

After 30 s, several patches of relatively high slip rate were resolved (Figure 1f). The first three patches were distributed between approximately 40 and 130 km east of the epicenter and peaked at about 33 s, 36 s, and 37 s, respectively (Figure 1f). The third patch, which peaked at approximately 37 s, extended from approximately 40 to 80 km east of the epicenter and was spatially separated from the apparent rupture front. Subsequent patches peaked at approximately 43, 51, and 57 s and were located near the apparent rupture front (Figure 1f).

4. Discussion

4.1. An integrated view of rupture propagation

Analyses based on seven different velocity-structure models consistently show three features of the source process (Figures 1f and S3 in the Supporting Information). First, the rupture propagated eastward at an average rate of 5–6 km/s, exceeding the S-wave velocity in the source region. Second, the eastward rupture stalled at about 50, 100, and 150 km east of the epicenter, with the apparent rupture front appearing to shift back by about 20 km during the final stall. Third, the slip rate peaked at about 37 s in a region approximately 90 km behind the apparent rupture front, closer to the epicenter.

We evaluated the fast rupture-front propagation by using the far-field surface waves. We compared vertical-component records filtered at 10–25 s from the 2026 doublet with those from the closely located M_W 6.4 event in 2009 (Text S1 in Supporting Information). The two events yield closely similar waveforms at azimuths of 35°–50°, approximately coinciding with the azimuthal range in which a Mach cone is expected for a rupture propagating at 5 km/s along an azimuth of 87° (Figure S7 in Supporting Information). Comparable behavior of Rayleigh waves has been reported for earthquakes identified as supershear (Bao et al., 2019, 2022; Hicks et al., 2020; Liu et al., 2023; Ren et al., 2024; Vallée & Dunham, 2012; Xu et al., 2025; Zhang et al., 2022).

To further examine the rapid eastward rupture propagation, the three apparent rupture stalls, and the spatially separated high-slip-rate subevent, we applied the hybrid back-projection (HBP) method (Yagi et al., 2012) to image the sources of seismic radiation associated with spatiotemporal variations in rupture-front velocity and slip rate (e.g., Madariaga, 1977; Madariaga et al., 2006; Spudich & Frazer, 1984). By using cross-correlation functions between the observed waveforms and Green's functions, the HBP method reduces the effects of reflected phases (e.g., pP and sP) and provides source images that can be directly compared with the PDTI results (Yagi and Okuwaki, 2015). We analyzed two frequency bands, 0.3–1.0 Hz and 0.1–0.3 Hz, chosen so that radiation from the rupture front and from the region of largest slip rate could be examined separately.

In the higher-frequency band, the major radiators are located near the apparent rupture front (Figure 3a). Distinct clusters are observed near the rupture stalls approximately 50 and 150 km east of the epicenter, with the latter accompanied by an apparent backward shift of the apparent rupture front. A weaker source cluster is also found between 30 and 40 s, about 90 km west of the apparent rupture front. In the low-frequency band, the sources are distributed mainly within the region of moderate or higher slip rate (Figure 3b). Distinct source clusters correspond to the rupture stall approximately 50 km east of the hypocenter, the subsequent rupture acceleration, and the acceleration following another stall approximately 100 km east of the hypocenter. A source cluster is also observed between 30 and 40 s, approximately 90 km west of the apparent rupture front.

The two frequency bands image different aspects of the same rupture process. Both reflect changes in rupture propagation or slip rate, with the high- and low-frequency sources likely emphasizing changes occurring over different temporal scales. Overall, the three rupture characteristics initially identified in the PDTI model are broadly reproduced by the HBP analysis, which does not explicitly assume a rupture velocity.

4.2. Rupture stalls and the estimated fault geometry

The rupture propagated through a transform-fault system composed of multiple structures rather than a single continuous fault. Within the source region, the rupture first followed the Boconó Fault, then the San Sebastián Fault, and farther east passed through the region where the Tacagua Fault and a submarine scarp appear to cross the San Sebastián Fault (Figures 1e and 2a). Each of the three rupture stalls identified above coincides with a change in fault geometry.

At the first stall, about 50 km east of the epicenter, the reduced strike of the PDTI solution rotates clockwise from approximately 85° to 90° along the Boconó Fault (Figures 1g and 2a). At the second stall, about 100 km east, it rotates counterclockwise from approximately 90° back to 85° along the San Sebastián Fault (Figures 1g and 2a). Both rotations coincide spatially with bends in the mapped fault traces (Alvarado et al., 2017; Styron & Pagani, 2020). Dynamic rupture simulations show that the geometric complexity of faults modulates the speed of the rupture front and can arrest it altogether (e.g., Ando & Kaneko, 2018; Aochi & Madariaga, 2003; Gabriel et al., 2023; Wang et al., 2023). The spatial correspondence suggests that the curvature of the Boconó and San Sebastián Faults regulated the passage of the rupture front.

The third stall, about 150 km east of the epicenter, is the most pronounced. It lasts longer than the first two stalls and is accompanied by larger changes in inferred strike and dip, from 85° to 92° and from 78° to 84°, respectively (Figures 1g and 1h). The HBP analysis reveals the strongest high-frequency radiation of the sequence between 34 and 50 s (Figure 3a). This stall occurs near the apparent intersection of the San Sebastián Fault with the Tacagua Fault and with a submarine scarp that may represent the northwestward offshore extension of the Tacagua Fault (Figures 1e and 1f).

It remains unclear whether the Tacagua Fault continues northwestward offshore as a submarine scarp physically connected to the San Sebastián Fault. A northwestward offshore extension of the Tacagua Fault has been proposed (Rial, 1973), but its intersection with the San Sebastián Fault remains uncertain (Audemard et al., 2000). Subject to these uncertainties, the most pronounced rupture stall occurs near the apparent intersection of these structures, suggesting that the local fault geometry played an important role in controlling rupture propagation through this region.

4.3. A complex rupture process during the doublet

Approximately 37 s after the origin time of the M_W 7.2 earthquake, a high-slip-rate subevent occurred approximately 90 km behind the leading rupture front, toward the initial epicenter (Figure 1f). This subevent was also identified by the HBP analysis in both the high- and low-frequency bands (Figure 3), and its timing was close to the cataloged origin time of the M_W 7.5 event.

Two interpretations may explain this spatially separated subevent: it may represent a back-propagating rupture from the preceding rupture front or a relatively independent rupture episode. Back-propagating ruptures with velocities approaching the local P-wave velocity have been reported for several previous earthquakes (e.g., Hicks et al., 2020; Inoue et al., 2025; Ren et al., 2024). Although the propagation is unclear in the snapshots of this study because the slip rate temporarily decreases, the large-slip region also appears to migrate toward the initial epicenter, at approximately 6 km/s, a velocity which is close to the P-wave velocity in the source region (Figures 1f and 2b).

In back-propagating ruptures reported for previous strike-slip earthquakes, the reverse migration was relatively continuous, and was also clearly imaged by BP analyses (e.g., Hicks et al., 2020; Inoue et al., 2025; Yao et al., 2025). Here, neither the PDTI nor the HBP analysis clearly resolves continuous westward migration (Figures 1f, 2, and 3). Our results therefore do not uniquely distinguish between back-propagating rupture and a spatially separated rupture episode.

Taking the high-slip-rate subevent at approximately 37 s as a possible starting point, subsequent high-slip-rate patches define an eastward migration consistent with an apparent velocity of approximately 6 km/s (Figure 1f). The low-frequency HBP result shows a similar eastward progression from this region (Figure 3b). These observations suggest that eastward supershear rupture initiated or resumed following the subevent.

The eastward rupture propagation is not continuous, however, and the source images instead show several intermittently activated patches. Apparent gaps occur approximately 75–90 km and 120–130 km east of the initial epicenter, in regions that had already experienced substantial slip during the preceding rupture (Figures 1f and 2).

These gaps may therefore reflect relatively weak additional slip through previously ruptured areas rather than complete rupture arrest, although the available resolution does not allow these possibilities to be distinguished.

Overall, the 2026 Venezuela earthquake involved predominantly eastward supershear rupture, temporary rupture stalls near changes in the inferred fault geometry, and a spatially separated high-slip-rate subevent. Rapid eastward rupture appears to have initiated or resumed following this subevent, and parts of the source region may have been traversed by two episodes of supershear rupture within less than one minute. This scenario raises the possibility of repeated strong shaking over the same region and may have implications for the duration and spatial extent of damaging ground motion.

5. Conclusion

We analyzed the rupture process of the 24 June 2026 Venezuela earthquake doublet using PDTI of teleseismic P waves. Analyses using seven structural models consistently showed that the rupture propagated mainly eastward over approximately 220 km, with rupture velocities exceeding the local S-wave speed during multiple stages. Three apparent rupture stalls were accompanied by changes in the inferred fault orientation, suggesting that fault bends or segment transitions may have influenced rupture propagation. A high-slip-rate subevent occurred approximately 37 s after the origin time of the first event, well behind the preceding apparent rupture front. The origin of this subevent remains ambiguous and may reflect either back-propagating rupture or a relatively independent rupture episode. Regardless of its origin, rapid eastward rupture propagation appears to have initiated or resumed after this subevent. These results reveal a compound rupture process involving multiple episodes of supershear propagation and interaction with complex fault geometry, with possible implications for repeated strong ground motion along transform-fault systems.

Conflict of Interest

The authors declare there are no conflicts of interest in this manuscript.

Open Research

All seismic waveform data used in the analyses were downloaded through the Wilber 3 system (https://ds.iris.edu/wilber3/) from the NSF NGF data archive operated by EarthScope Consortium (NSF award 2435260). The following seismic networks were used: (1) CNSN, https://doi.org/10.7914/SN/CN (2) GEOSCOPE, https://doi.org/10.18715/GEOSCOPE.G (3) GEOFON, https://doi.org/10.14470/TR560404 (4) GTSN, https://doi.org/10.7914/SN/GT (5) GSN/II, https://doi.org/10.7914/SN/II (6) IM, https://doi.org/10.7914/vefq-vh75 (7) GSN, https://doi.org/10.7914/SN/IU (8) MedNet, https://doi.org/10.13127/sd/fbbbtdtd6q and (9) NSAN, https://doi.org/10.21944/e970fd34-23b9-3411-b366-e4f72877d2c5. The aftershock distribution used in this study was obtained from the U.S. Geological Survey Advanced National Seismic System Comprehensive Earthquake Catalog (ComCat; https://doi.org/10.5066/F7MS3QZH) and the FUNVISIS Observatorio Nacional de Sismos (http://www.funvisis.gob.ve/monitor.html). Global Centroid Moment Tensor (GCMT) solutions were obtained from the GCMT catalog (https://www.globalcmt.org/CMTsearch.html). Plate-boundary data were obtained from the PB2002 digital plate-boundary model (Bird, 2003). Plate motion data were obtained using the Plate Motion Calculator (http://ofgs.aori.u-tokyo.ac.jp/~okino/platecalc_new.html) with plate-motion model of DeMets et al. (2010). Bathymetric and topographic data were obtained from the GEBCO_2026 Grid (GEBCO Bathymetric Compilation Group 2026, 2026), available at https://download.gebco.net/. The CRUST1.0 and ak135-F are available through the websites https://igppweb.ucsd.edu/~gabi/crust1.html and http://rses.anu.edu.au/seismology/ak135/ak135f.html. We used the Generic Mapping Tools (v6.6.0; https://www.generic-mapping-tools.org; Wessel et al., 2019; Wessel et al., 2025), Cartopy (Elson et al., 2022), ObsPy (Beyreuther et al., 2010; The ObsPy Development Team, 2022), Pyrocko (Heimann et al., 2017), matplotlib (Caswell et al., 2022; Hunter, 2007), and Scientific color maps (https://www.fabiocrameri.ch/colourmaps/; Crameri, 2018; Crameri et al., 2020) for data processing and visualization.

Acknowledgement

We employed FPSPACK (Gasperini & Vannucci, 2003) to manage the focal mechanisms derived from the inversion analysis. This work was supported by JSPS KAKENHI Grant Numbers 25K01075, 26KJ0633, 24H01020 ("Science of Slow-to-Fast Earthquakes”), and 26K07241. Tuncay Taymaz acknowledges support from Istanbul Technical University (ITU-BAP through PEDAP project PMA-2025-47868), and Disaster Management Institute (ITU-AYE). The authors acknowledge Ryosuke Ando for the fruitful discussion.

Use of Generative Artificial Intelligence

We used ChatGPT (OpenAI, GPT-5.6) for English-language editing and coding support. We reviewed and verified all AI-assisted text and code and take full responsibility for the final content.

Reference

Abdelmeguid, M., Zhao, C., Yalcinkaya, E., Gazetas, G., Elbanna, A., & Rosakis, A. (2023). Dynamics of episodic supershear in the 2023 M7.8 Kahramanmaraş/Pazarcik earthquake, revealed by near-field records and computational modeling. *Communications Earth & Environment*, *4*(1), 456. https://doi.org/10.1038/s43247-023-01131-7

Akaike, H. (1980). Likelihood and the Bayes procedure. *Trabajos de Estadistica Y de Investigacion Operativa*, *31*(1), 143–166. https://doi.org/10.1007/BF02888350

Alvarado, A., Audemard, F., Benavente Escobar, C., Santibanez Boric, I., Cembrano Perasso, J., Costa, C., et al. (2017). the South American Risk Assessment Active Fault Database [Data set]. GEM Foundation. https://doi.org/10.13117/SARA-ACTIVE-FAULTS

Ando, R., & Kaneko, Y. (2018). Dynamic Rupture Simulation Reproduces Spontaneous Multifault Rupture and Arrest During the 2016 M_{w} 7.9 Kaikoura Earthquake. *Geophysical Research Letters*, *45*(23). https://doi.org/10.1029/2018GL080550

Aochi, H., & Madariaga, R. (2003). The 1999 Izmit, Turkey, Earthquake: Nonplanar Fault Structure, Dynamic Rupture Process, and Strong Ground Motion. *Bulletin of the Seismological Society of America*, *93*(3), 1249–1266. https://doi.org/10.1785/0120020167

Archuleta, R. J. (1984). A faulting model for the 1979 Imperial Valley earthquake. *Journal of Geophysical Research: Solid Earth*, *89*(B6), 4559–4585. https://doi.org/10.1029/JB089iB06p04559

Audemard, F. A. (2003). Geomorphic and geologic evidence of ongoing uplift and deformation in the Mérida Andes, Venezuela. *Quaternary International*, *101–102*, 43–65. https://doi.org/10.1016/S1040-6182(02)00128-3

Audemard, F. A., Machette, M., Cox, J. W., Dart, R. L., & Haller, K. (2000). *Map and database of Quaternary faults in Venezuela and its offshore regions* (Report No. 2000–18). Reston, VA. https://doi.org/10.3133/ofr0018

Audemard, F. A. (2007). Revised seismic history of the El Pilar fault, Northeastern Venezuela, from the Cariaco 1997 earthquake and recent preliminary paleoseismic results. *Journal of Seismology*, *11*(3), 311–326. https://doi.org/10.1007/s10950-007-9054-2

Audemard, F. A., Alvarado, L., Arnaiz, M., Romero, G., Reinoza-Gómez, C. E., Martínez-González, A. I., et al. (2025). Sismicidad de profundidad intermedia de la losa de subducción de las Antillas menores, próxima a la península de Paria, Venezuela. *Boletín de Geología*, *47*(1). https://doi.org/10.18273/revbol.v47n1-2025005

Bao, H., Ampuero, J.-P., Meng, L., Fielding, E. J., Liang, C., Milliner, C. W. D., et al. (2019). Early and persistent supershear rupture of the 2018 magnitude 7.5 Palu earthquake. *Nature Geoscience*, *12*(3), 200–205. https://doi.org/10.1038/s41561-018-0297-z

Bao, H., Xu, L., Meng, L., Ampuero, J.-P., Gao, L., & Zhang, H. (2022). Global frequency of oceanic and continental supershear earthquakes. *Nature Geoscience*, *15*(11), 942–949. https://doi.org/10.1038/s41561-022-01055-5

Beyreuther, M., Barsch, R., Krischer, L., Megies, T., Behr, Y., & Wassermann, J. (2010). ObsPy: A Python Toolbox for Seismology. *Seismological Research Letters*, *81*(3), 530–533. https://doi.org/10.1785/gssrl.81.3.530

Bird, P. (2003). An updated digital model of plate boundaries: UPDATED MODEL OF PLATE BOUNDARIES. *Geochemistry, Geophysics, Geosystems*, *4*(3). https://doi.org/10.1029/2001GC000252

Bouchon, M., Karabulut, H., Bouin, M.-P., Schmittbuhl, J., Vallée, M., Archuleta, R., et al. (2010). Faulting characteristics of supershear earthquakes. *Tectonophysics*, *493*(3–4), 244–253. https://doi.org/10.1016/j.tecto.2010.06.011

Bouin, M.-P., Bouchon, M., Karabulut, H., & Aktar, M. (2004). Rupture process of the 1999 November 12 Düzce (Turkey) earthquake deduced from strong motion and Global Positioning System measurements. *Geophysical Journal International*, *159*(1), 207–211. https://doi.org/10.1111/j.1365-246X.2004.02367.x

Caswell, T. A., Lee, A., Droettboom, M., De Andrade, E. S., Hoffmann, T., Klymak, J., et al. (2022, August 11). matplotlib/matplotlib: REL: v3.5.3 (Version v3.5.3). Zenodo. https://doi.org/10.5281/ZENODO.6982547

Choy, J. E., Palme, C., Guada, C., Morandi, M., & Klarica, S. (2010). Macroseismic Interpretation of the 1812 Earthquakes in Venezuela Using Intensity Uncertainties and A Priori Fault-Strike Information. *Bulletin of the Seismological Society of America*, *100*(1), 241–255. https://doi.org/10.1785/0120080345

Colón, S., Audemard, F. A., Beck, C., Avila, J., Padrón, C., De Batist, M., et al. (2015). The 1900 Mw 7.6 earthquake offshore north–central Venezuela: Is La Tortuga or San Sebastián the source fault? *Marine and Petroleum Geology*, *67*, 498–511. https://doi.org/10.1016/j.marpetgeo.2015.06.005

Crameri, F. (2018). Geodynamic diagnostics, scientific visualisation and StagLab 3.0. *Geoscientific Model Development*, *11*(6), 2541–2562. https://doi.org/10.5194/gmd-11-2541-2018

Crameri, F., Shephard, G. E., & Heron, P. J. (2020). The misuse of colour in science communication. *Nature Communications*, *11*(1), 5444. https://doi.org/10.1038/s41467-020-19160-7

Crotwell, H. P., Owens, T. J., & Ritsema, J. (1999). The TauP Toolkit: Flexible Seismic Travel-time and Ray-path Utilities. *Seismological Research Letters*, *70*(2), 154–160. https://doi.org/10.1785/gssrl.70.2.154

DeMets, C., Gordon, R. G., & Argus, D. F. (2010). Geologically current plate motions. *Geophysical Journal*

International, *181*(1), 1–80. https://doi.org/10.1111/j.1365-246X.2009.04491.x

Dewey, J. W. (1972). Seismicity and tectonics of western Venezuela. *Bulletin of the Seismological Society of America*, *62*(6), 1711–1751. https://doi.org/10.1785/BSSA0620061711

Dunham, E. M., & Archuleta, R. J. (2004). Evidence for a Supershear Transient during the 2002 Denali Fault Earthquake. *Bulletin of the Seismological Society of America*, *94*(6B), S256–S268. https://doi.org/10.1785/0120040616

Dziewonski, A. M., Chou, T.-A., & Woodhouse, J. H. (1981). Determination of earthquake source parameters from waveform data for studies of global and regional seismicity. *Journal of Geophysical Research: Solid Earth*, *86*(B4), 2825–2852. https://doi.org/10.1029/JB086iB04p02825

Ekström, G., Nettles, M., & Dziewoński, A. M. (2012). The global CMT project 2004–2010: Centroid-moment tensors for 13,017 earthquakes. *Physics of the Earth and Planetary Interiors*, *200–201*, 1–9. https://doi.org/10.1016/j.pepi.2012.04.002

Elson, P., De Andrade, E. S., Lucas, G., May, R., Hattersley, R., Campbell, E., et al. (2022). SciTools/cartopy: v0.21.1 (Version v0.21.1). Zenodo. https://doi.org/10.5281/ZENODO.7430317

FUNVISIS. (2026). Observatorio Nacional de Sismos. Retrieved from http://www.funvisis.gob.ve/monitor.html

Gabriel, A.-A., Ulrich, T., Marchandon, M., Biemiller, J., & Rekoske, J. (2023). 3D Dynamic Rupture Modeling of the 6 February 2023, Kahramanmaraş, Turkey Mw 7.8 and 7.7 Earthquake Doublet Using Early Observations. *The Seismic Record*, *3*(4), 342–356. https://doi.org/10.1785/0320230028

Gasperini, P., & Vannucci, G. (2003). FPSPACK: a package of FORTRAN subroutines to manage earthquake focal mechanism data. *Computers & Geosciences*, *29*(7), 893–901. https://doi.org/10.1016/S0098-3004(03)00096-7

GEBCO Bathymetric Compilation Group 2026. (2026). The GEBCO_2026 Grid - a continuous terrain model for oceans and land at 15 arc-second intervals. (Version 8) [Geographic Information System,Network Common Data Form,Text or Plaintext]. NERC EDS British Oceanographic Data Centre NOC. https://doi.org/10.5285/4F68D5C7-45EB-F999-E063-7086ABC036FA

Heimann, S., Kriegerowski, M., Isken, M., Cesca, S., Daout, S., Grigoli, F., et al. (2017). Pyrocko - An open-source seismology toolbox and library. GFZ Data Services. https://doi.org/10.5880/GFZ.2.1.2017.001

Hicks, S. P., Okuwaki, R., Steinberg, A., Rychert, C. A., Harmon, N., Abercrombie, R. E., et al. (2020). Back-propagating supershear rupture in the 2016 Mw 7.1 Romanche transform fault earthquake. *Nature Geoscience*, *13*(9), 647–653. https://doi.org/10.1038/s41561-020-0619-9

Hunter, J. D. (2007). Matplotlib: A 2D Graphics Environment. *Computing in Science & Engineering*, *9*(3), 90–95. https://doi.org/10.1109/MCSE.2007.55

Inoue, N., Yamaguchi, R., Yagi, Y., Okuwaki, R., Bogdan, E., & Tadapansawut, T. (2025). A multiple asymmetric bilateral rupture sequence derived from the peculiar tele-seismic P-waves of the 2025 Mandalay, Myanmar earthquake. *Seismica*, *4*(1). https://doi.org/10.26443/seismica.v4i1.1691

Jia, Z., Jin, Z., Marchandon, M., Ulrich, T., Gabriel, A.-A., Fan, W., et al. (2023). The complex dynamics of the 2023 Kahramanmaraş, Turkey, M_w 7.8-7.7 earthquake doublet. *Science*, *381*(6661), 985–990. https://doi.org/10.1126/science.adi0685

Kennett, B. L. N., Engdahl, E. R., & Buland, R. (1995). Constraints on seismic velocities in the Earth from traveltimes. *Geophysical Journal International*, *122*(1), 108–124. https://doi.org/10.1111/j.1365-246X.1995.tb03540.x

Kikuchi, M., & Kanamori, H. (1991). Inversion of complex body waves—III. *Bulletin of the Seismological Society of America*, *81*(6), 2335–2350. https://doi.org/10.1785/BSSA0810062335

Laske, G., Masters, G., Ma, Z., & Pasyanos, M. (2013). Update on CRUST1.0 - A 1-degree Global Model of Earth's Crust, EGU2013-2658. Presented at the EGU General Assembly Conference Abstracts.

Liu, C., Lay, T., Wang, R., Taymaz, T., Xie, Z., Xiong, X., et al. (2023). Complex multi-fault rupture and triggering during the 2023 earthquake doublet in southeastern Türkiye. *Nature Communications*, *14*(1), 5564. https://doi.org/10.1038/s41467-023-41404-5

Liu, C., Bai, Y., Lay, T., He, P., Wen, Y., Xiong, X., Taymaz, T. (2026). Simple Unilateral Rupture of the Great Mw 8.8 2025 Kamchatka Earthquake. *Science*, 391(6787), 812-817. https://www.science.org/doi/10.1126/science.aeb8232.

Madariaga, R. (1977). High-frequency radiation from crack (stress drop) models of earthquake faulting. *Geophysical Journal International*, *51*(3), 625–651. https://doi.org/10.1111/j.1365-246X.1977.tb04211.x

Madariaga, R., Ampuero, J., & Adda-Bedia, M. (2006). Seismic radiation from simple models of earthquakes. *GEOPHYSICAL MONOGRAPH-AMERICAN GEOPHYSICAL UNION*, *170*, 223.

Mai, P. M., Schorlemmer, D., Page, M., Ampuero, J., Asano, K., Causse, M., et al. (2016). The Earthquake-Source Inversion Validation (SIV) Project. *Seismological Research Letters*, *87*(3), 690–708. https://doi.org/10.1785/0220150231

Montagner, J.-P., & Kennett, B. L. N. (1996). How to reconcile body-wave and normal-mode reference earth models.

Geophysical Journal International, *125*(1), 229–248. https://doi.org/10.1111/j.1365-246X.1996.tb06548.x

NASA Earth Observatory. (2026). Where Venezuela's Earthquakes Shifted the Ground. Retrieved from https://science.nasa.gov/earth/earth-observatory/where-venezuelas-earthquakes-shifted-the-ground/

Ohara, K., Yagi, Y., Yamashita, S., Okuwaki, R., Hirano, S., & Fukahata, Y. (2023). Complex evolution of the 2016 Kaikoura earthquake revealed by teleseismic body waves. *Progress in Earth and Planetary Science*, *10*(1), 35. https://doi.org/10.1186/s40645-023-00565-z

Okuwaki, R., Hirano, S., Yagi, Y., & Shimizu, K. (2020). Inchworm-like source evolution through a geometrically complex fault fueled persistent supershear rupture during the 2018 Palu Indonesia earthquake. *Earth and Planetary Science Letters*, *547*, 116449. https://doi.org/10.1016/j.epsl.2020.116449

Okuwaki, R., Hicks, S. P., Craig, T. J., Fan, W., Goes, S., Wright, T. J., & Yagi, Y. (2021). Illuminating a Contorted Slab With a Complex Intraslab Rupture Evolution During the 2021 Mw 7.3 East Cape, New Zealand Earthquake. *Geophysical Research Letters*, *48*(24), e2021GL095117. https://doi.org/10.1029/2021GL095117

Okuwaki, R., Yagi, Y., Taymaz, T., & Hicks, S. P. (2023). Multi-Scale Rupture Growth With Alternating Directions in a Complex Fault Network During the 2023 South-Eastern Türkiye and Syria Earthquake Doublet. *Geophysical Research Letters*, *50*(12), e2023GL103480. https://doi.org/10.1029/2023GL103480

Paige, S. (1930). The earthquake at Cumana, Venezuela, January 17, 1929. *Bulletin of the Seismological Society of America*, *20*(1), 1–10. https://doi.org/10.1785/BSSA0200010001

Pousse-Beltran, L., Vassallo, R., Audemard, F., Jouanne, F., Carcaillet, J., Pathier, E., & Volat, M. (2017). Pleistocene slip rates on the Boconó fault along the North Andean Block plate boundary, Venezuela. *Tectonics*, *36*(7), 1207–1231. https://doi.org/10.1002/2016TC004305

Pousse-Beltran, L., Vassallo, R., Audemard, F., Jouanne, F., Oropeza, J., Garambois, S., & Aray, J. (2018). Earthquake geology of the last millennium along the Boconó Fault, Venezuela. *Tectonophysics*, *747–748*, 40–53. https://doi.org/10.1016/j.tecto.2018.09.010

Ragon, T., Sladen, A., & Simons, M. (2018). Accounting for uncertain fault geometry in earthquake source inversions – I: theory and simplified application. *Geophysical Journal International*, *214*(2), 1174–1190. https://doi.org/10.1093/gji/ggy187

Ren, C., Wang, Z., Taymaz, T., Hu, N., Luo, H., Zhao, Z., et al. (2024). Supershear triggering and cascading fault ruptures of the 2023 Kahramanmaraş, Türkiye, earthquake doublet. *Science*, *383*(6680), 305–311. https://doi.org/10.1126/science.adi1519

Rial, J. A. (1973). La fosa tectónica de Tacagua y su relación con la sismicidad de la región de Caracas. *Bol. Soc. Ven. Geol.*, *v. 8*(N° 3), 49–54.

Sato, D. S. K., Fukahata, Y., & Nozue, Y. (2022). Appropriate reduction of the posterior distribution in fully Bayesian inversions. *Geophysical Journal International*, *231*(2), 950–981. https://doi.org/10.1093/gji/ggac231

Sato, D. S. K., Yagi, Y., Okuwaki, R., & Fukahata, Y. (2026). Smooth surface reconstruction of earthquake faults from distributed moment-potency-tensor solutions. *Geophysical Journal International*, *245*(3), ggag116. https://doi.org/10.1093/gji/ggag116

Shimizu, K., Yagi, Y., Okuwaki, R., & Fukahata, Y. (2020). Development of an inversion method to extract information on fault geometry from teleseismic data. *Geophysical Journal International*, *220*(2), 1055–1065. https://doi.org/10.1093/gji/ggz496

Shimizu, K., Yagi, Y., Okuwaki, R., & Fukahata, Y. (2021). Construction of fault geometry by finite-fault inversion of teleseismic data. *Geophysical Journal International*, *224*(2), 1003–1014. https://doi.org/10.1093/gji/ggaa501

Styron, R., & Pagani, M. (2020). The GEM Global Active Faults Database. *Earthquake Spectra*, *36*(1_suppl), 160–180. https://doi.org/10.1177/8755293020944182

Spudich, P., & Frazer, L. N. (1984). Use of ray theory to calculate high-frequency radiation from earthquake sources having spatially variable rupture velocity and stress drop. *Bulletin of the Seismological Society of America*, *74*(6), 2061–2082. https://doi.org/10.1785/BSSA0740062061

Tadapansawut, T., Okuwaki, R., Yagi, Y., & Yamashita, S. (2021). Rupture Process of the 2020 Caribbean Earthquake Along the Oriente Transform Fault, Involving Supershear Rupture and Geometric Complexity of Fault. *Geophysical Research Letters*, *48*(1). https://doi.org/10.1029/2020GL090899

The ObsPy Development Team. (2022). ObsPy 1.4.0 (Version 1.4.0). Zenodo. https://doi.org/10.5281/ZENODO.6645832

USGS. (2017). Advanced National Seismic System (ANSS) Comprehensive Catalog. https://doi.org/10.5066/F7MS3QZH

USGS. (2026a). M 7.2 - 21 km ENE of San Felipe, Venezuela. Retrieved from https://earthquake.usgs.gov/earthquakes/eventpage/us6000t7zc/executive

USGS. (2026b). M 7.5 - 20 km ESE of Yumare, Venezuela. Retrieved from https://earthquake.usgs.gov/earthquakes/eventpage/us6000t7zp/executive

Vallée, M., & Dunham, E. M. (2012). Observation of far-field Mach waves generated by the 2001 Kokoxili supershear earthquake. *Geophysical Research Letters*, *39*(5), 2011GL050725. https://doi.org/10.1029/2011GL050725

Vallée, M., Landès, M., Shapiro, N. M., & Klinger, Y. (2008). The 14 November 2001 Kokoxili (Tibet) earthquake: High-frequency seismic radiation originating from the transitions between sub-Rayleigh and supershear rupture velocity regimes. *Journal of Geophysical Research: Solid Earth*, *113*(B7), 2007JB005520. https://doi.org/10.1029/2007JB005520

Wang, Z., Zhang, W., Taymaz, T., He, Z., Xu, T., & Zhang, Z. (2023). Dynamic Rupture Process of the 2023 *Mw* 7.8 Kahramanmaraş Earthquake (SE Türkiye): Variable Rupture Speed and Implications for Seismic Hazard. *Geophysical Research Letters*, *50*(15), e2023GL104787. https://doi.org/10.1029/2023GL104787

Wessel, P., Luis, J. F., Uieda, L., Scharroo, R., Wobbe, F., Smith, W. H. F., & Tian, D. (2019). The Generic Mapping Tools Version 6. *Geochemistry, Geophysics, Geosystems*, *20*(11), 5556–5564. https://doi.org/10.1029/2019GC008515

Wessel, Paul, Luis, J. F., Uieda, L., Scharroo, R., Wobbe, F., Smith, W. H. F., et al. (2025, July 26). The Generic Mapping Tools version 6.6.0 (Version 6.6.0). Zenodo. https://doi.org/10.5281/ZENODO.16448627

Xu, L., Meng, L., Yunjun, Z., Yang, Y., Wang, Y., Hu, C., et al. (2025). Bimaterial effect and favorable energy ratio enabled supershear rupture in the 2025 Mandalay earthquake. *Science*, *390*(6772), 476–481. https://doi.org/10.1126/science.ady6100

Yabuki, T., & Matsu'ura, M. (1992). Geodetic data inversion using a Bayesian information criterion for spatial distribution of fault slip. *Geophysical Journal International*, *109*(2), 363–375. https://doi.org/10.1111/j.1365-246X.1992.tb00102.x

Yagi, Y., & Fukahata, Y. (2011). Introduction of uncertainty of Green's function into waveform inversion for seismic source processes: Uncertainty of Green's function in inversion. *Geophysical Journal International*, *186*(2), 711–720. https://doi.org/10.1111/j.1365-246X.2011.05043.x

Yagi, Y., Nakao, A., & Kasahara, A. (2012). Smooth and rapid slip near the Japan Trench during the 2011 Tohoku-oki earthquake revealed by a hybrid back-projection method. *Earth and Planetary Science Letters*, *355–356*, 94–101. https://doi.org/10.1016/j.epsl.2012.08.018

Yagi, Y., & Okuwaki, R. (2015). Integrated seismic source model of the 2015 Gorkha, Nepal, earthquake. *Geophysical Research Letters*, *42*(15), 6229–6235. https://doi.org/10.1002/2015GL064995

Yagi, Y., Okuwaki, R., Enescu, B., & Lu, J. (2023). Irregular rupture process of the 2022 Taitung, Taiwan, earthquake sequence. *Scientific Reports*, *13*(1), 1107. https://doi.org/10.1038/s41598-023-27384-y

Yamaguchi, R., Yagi, Y., Okuwaki, R., & Enescu, B. (2025). The complex rupture evolution of the long and slow, tsunamigenic 2021 South Sandwich Islands earthquake. *Scientific Reports*, *15*(1), 17706. https://doi.org/10.1038/s41598-025-02043-6

Yamashita, S., Yagi, Y., Okuwaki, R., Shimizu, K., Agata, R., & Fukahata, Y. (2021). Consecutive ruptures on a complex conjugate fault system during the 2018 Gulf of Alaska earthquake. *Scientific Reports*, *11*(1), 5979. https://doi.org/10.1038/s41598-021-85522-w

Yamashita, S., Yagi, Y., Okuwaki, R., Shimizu, K., Agata, R., & Fukahata, Y. (2022). Potency density tensor inversion of complex body waveforms with time-adaptive smoothing constraint. *Geophysical Journal International*, ggac181. https://doi.org/10.1093/gji/ggac181

Yao, Q., Yu, C., & Zhou, M. (2025). Bilateral Supershear Rupture of the 2025 M_W 7.7 Myanmar Earthquake Imaged by Global *P* -Wave and Regional Surface-Wave Back-Projections. *Geophysical Research Letters*, *52*(20), e2025GL116800. https://doi.org/10.1029/2025GL116800

Zhang, X., Feng, W., Du, H., Samsonov, S., & Yi, L. (2022). Supershear Rupture During the 2021 M_W 7.4 Maduo, China, Earthquake. *Geophysical Research Letters*, *49*(6), e2022GL097984. https://doi.org/10.1029/2022GL097984

Zhang, Y., Tang, X., Liu, D., Taymaz, T., Eken, T., Guo, R., et al. (2023). Geometric controls on cascading rupture of the 2023 Kahramanmaraş earthquake doublet. *Nature Geoscience*, *16*(11), 1054–1060. https://doi.org/10.1038/s41561-023-01283-3

Zhou, J., Xu, Y., Zhang, Y., Feng, W., Taymaz, T., Chen, Y.-T., et al. (2025). Geometric barriers impacted rupture processes and stress releases of the 2023 Kahramanmaraş, Türkiye, earthquake doublet. *Communications Earth & Environment*, *6*(1), 56. https://doi.org/10.1038/s43247-025-02004-x

References From the Supporting Information

Ekström, G. (2011). A global model of Love and Rayleigh surface wave dispersion and anisotropy, 25-250 s: Global dispersion model GDM52. *Geophysical Journal International*, *187*(3), 1668–1686. https://doi.org/10.1111/j.1365-246X.2011.05225.x

Ishii, M., Shearer, P. M., Houston, H., & Vidale, J. E. (2005). Extent, duration and speed of the 2004 Sumatra–Andaman earthquake imaged by the Hi-Net array. *Nature*, *435*(7044), 933–936.

https://doi.org/10.1038/nature03675

Krüger, F., & Ohrnberger, M. (2005). Tracking the rupture of the Mw = 9.3 Sumatra earthquake over 1,150 km at teleseismic distance. *Nature*, *435*(7044), 937–939. https://doi.org/10.1038/nature03696

Okuwaki, R., Yagi, Y., & Hirano, S. (2014). Relationship between High-frequency Radiation and Asperity Ruptures, Revealed by Hybrid Back-projection with a Non-planar Fault Model. *Scientific Reports*, *4*(1), 7120. https://doi.org/10.1038/srep07120

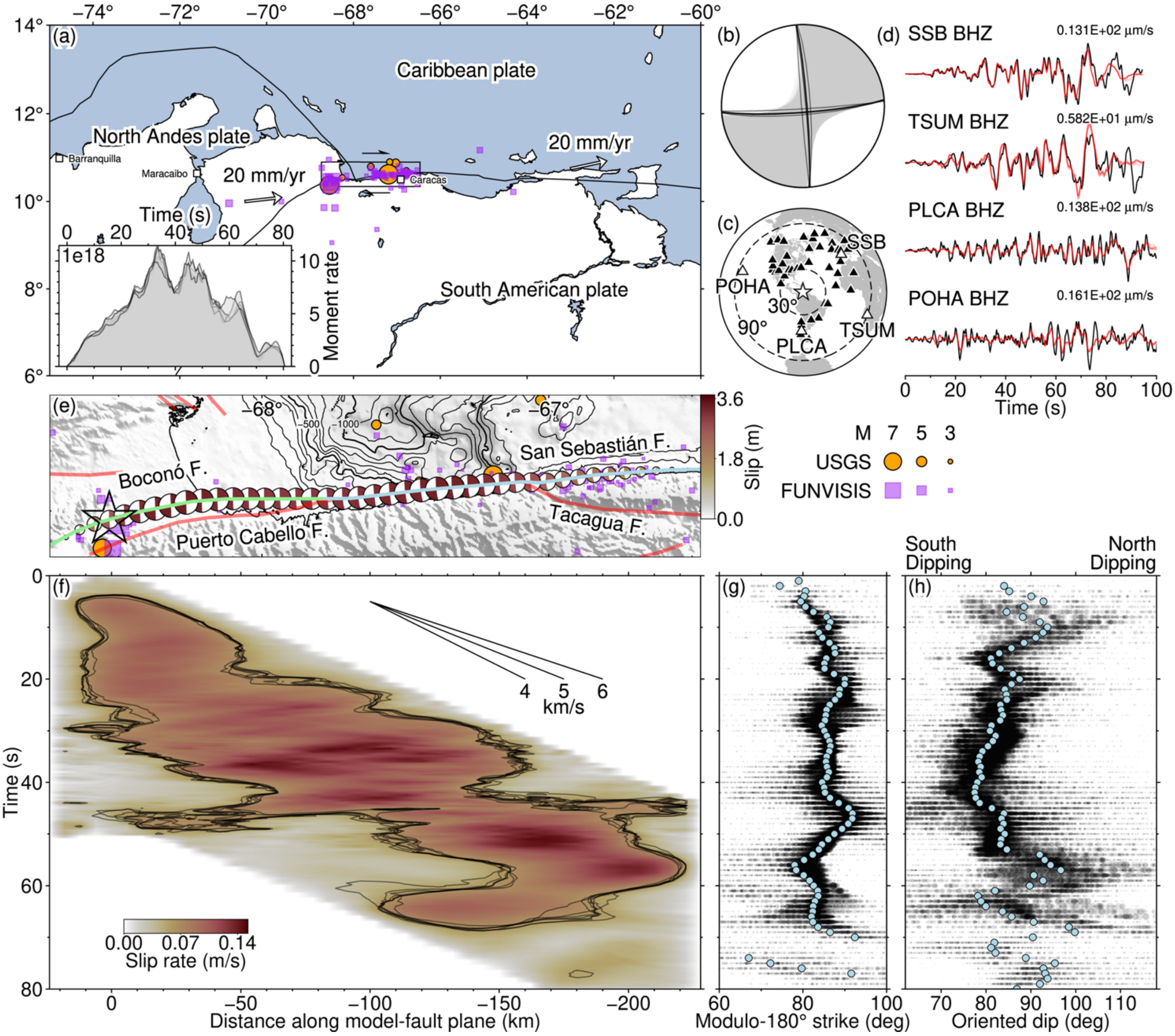

Figure 1

Study region and overview. (a) Regional map with the aftershocks during the first three days. The black line denotes the plate boundary. The arrows indicate the relative plate motion. The black rectangle delineates the area shown in panel (e). The inset shows the moment-rate functions calculated from the seven models. (b) The moment tensor solutions estimated from the seven models. (c) The station distribution used in the PDTI and the HBP method. (d) Selected traces of the observed (black) and synthetic (red) waveforms (white triangles in Figure 1c). The maximum amplitude of the observed trace is on the right of each panel. (e) Map projection of the median distribution of slip and focal mechanisms. The focal mechanisms associated with larger slip are plotted on top. The star indicates the rupture initiation point. The colored lines indicate the active faults (Styron & Pagani, 2020). (f) Spatiotemporal distribution of the median slip rate projected with the strike direction of the model plane as the horizontal axis. The black lines indicate the 40% contours of the maximum slip rate for each of the seven models. (g) The temporal variation of the modulo-180° strike. (h) The temporal variation of the oriented dip. In (g) and (h), the blue dots represent the median value.

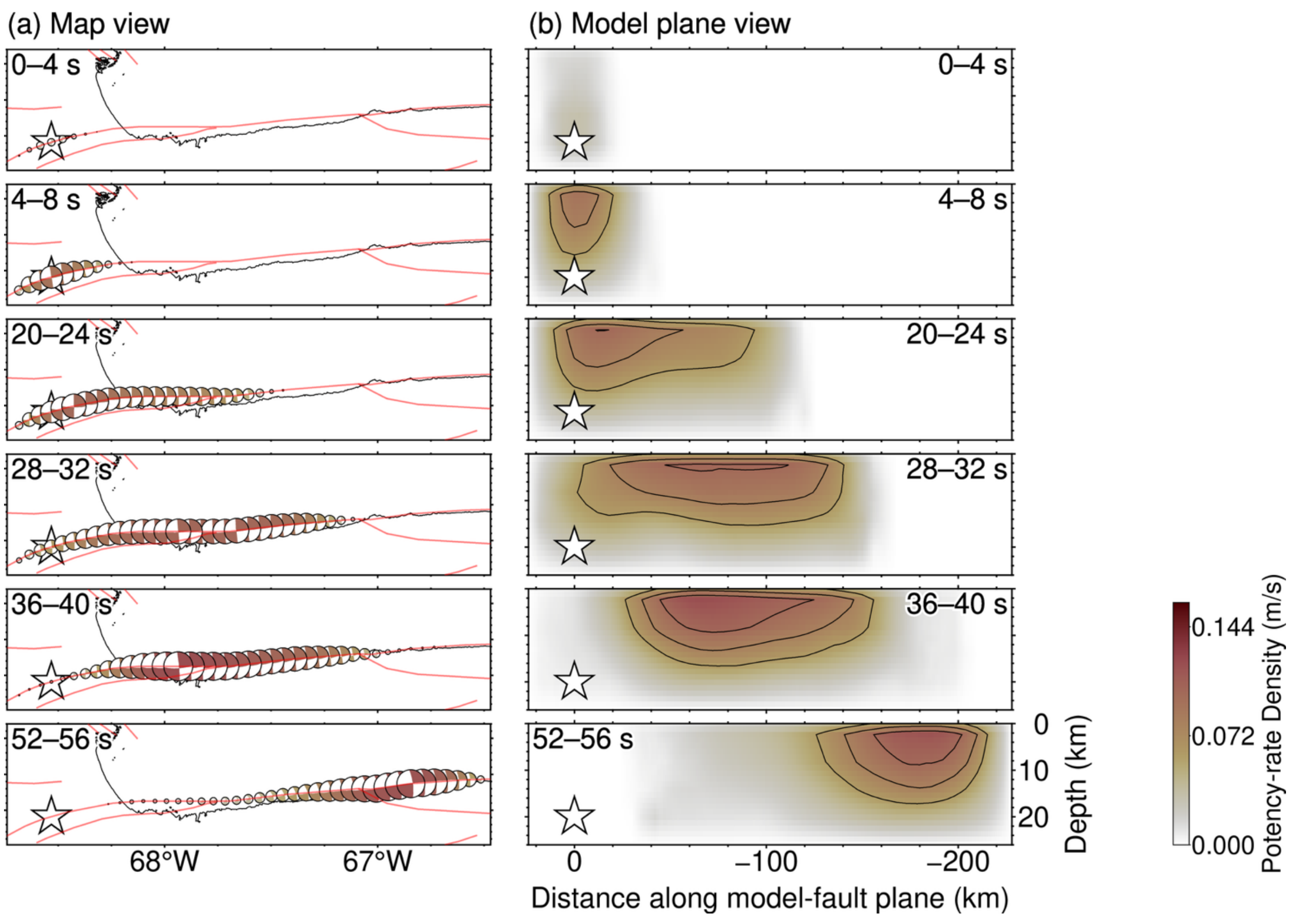

Figure 2

Selected snapshots of the rupture evolution. (a) Map projection of the focal mechanisms. The beachballs show focal mechanisms calculated from the median strike, dip, and rake values across the seven models. The colors and sizes of the beachballs represent the median slip rate across the seven models. The white star indicates the initial rupture point. The red lines show the active-fault models (Styron & Pagani, 2020). (b) Projection of the slip rate onto the model plane. The contour interval is 0.02 m/s.

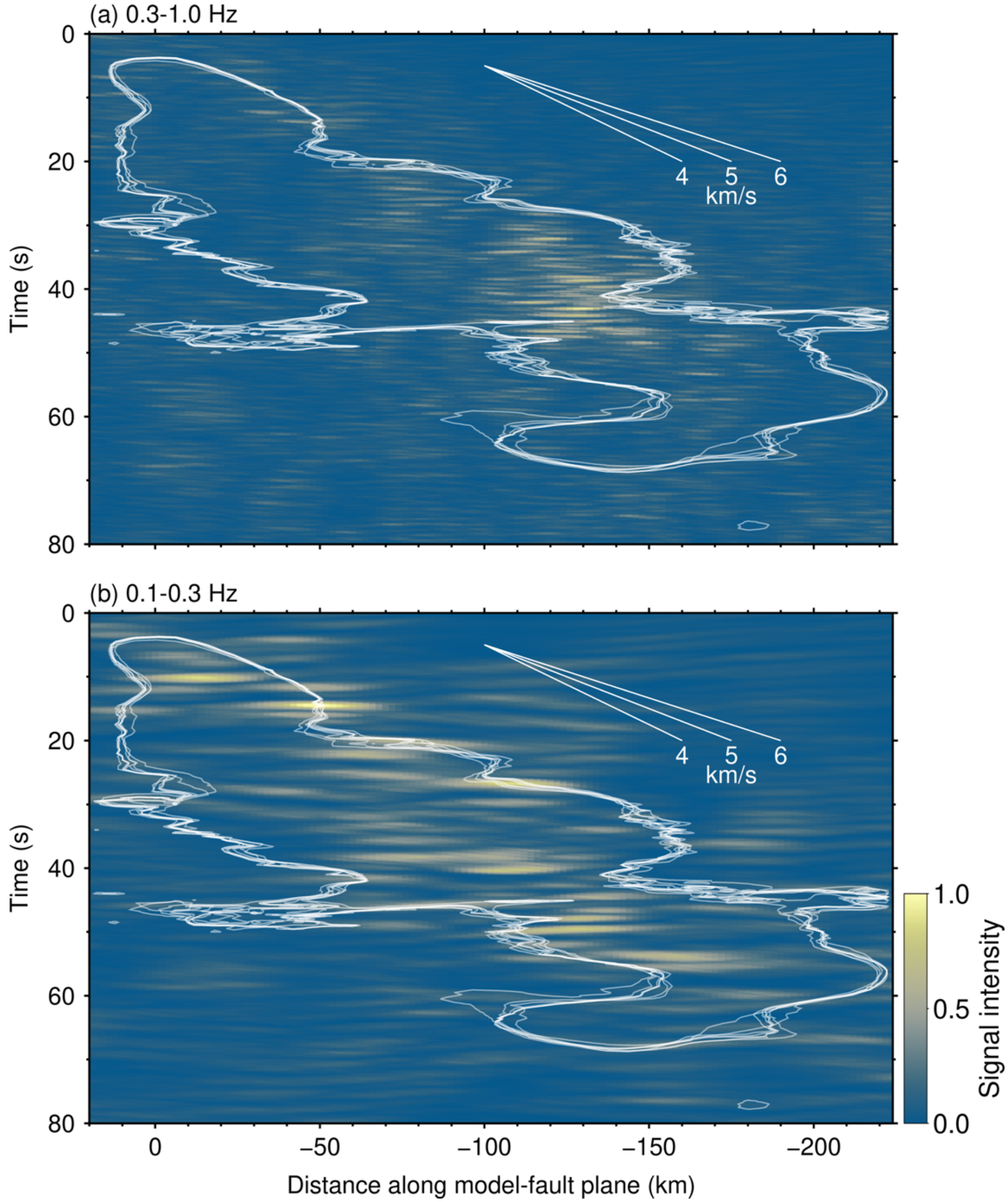

Figure 3

Comparison of the slip rate and the HBP images of the (a) high-frequency (0.3–1.0 Hz) and (b) low-frequency (0.1–0.3 Hz) bands. Colors indicate normalized signal intensity. The white contours show the 40% contours of the slip-rate distribution for each of the seven PDTI models.

Supporting information for

Compound Supershear Rupture During the 2026 Venezuela Earthquake Doublet

Ryo Yamaguchi[1,*], Naohiro Inoue[1], Takeshi Saito[2], Hayato Tanaka[2], Nozomi Ishida[1], Bogdan Enescu[3,4], Tuncay Taymaz[5,6], Ryo Okuwaki[7] and Yuji Yagi[7,*]

[1] Graduate School of Science and Technology, University of Tsukuba, Ten'nodai 1-1-1, Tsukuba, 305–8572, Ibaraki, Japan

[2] School of Life and Environmental Sciences, University of Tsukuba, Ten'nodai 1-1-1, Tsukuba, 305-8572, Ibaraki, Japan

[3] Department of Geophysics, Graduate School of Science, Kyoto University, Kitashirakawa, Oiwake-cho, Sakyo-ku, Kyoto 606-8502, Japan

[4] National Institute for Earth Physics, Calugareni str. 12, P.O. Box MG-2, Magurele-Bucharest, Ilfov, 077125, Romania

[5] Department of Geophysical Engineering, The Faculty of Mines, İstanbul Technical University, İTÜ Maslak Campus, Sarıyer 34469, İstanbul, Türkiye

[6] Disaster Management Institute, İstanbul Technical University, İTÜ Maslak Campus, Sarıyer 34469, İstanbul, Türkiye

[7] Institute of Life and Environmental Sciences, University of Tsukuba, Ten'nodai 1-1-1, Tsukuba, 305–8572, Ibaraki, Japan

[*]Corresponding Authors: Ryo Yamaguchi (yama0109@geol.tsukuba.ac.jp) and
Yuji Yagi (yagi-y@geol.tsukuba.ac.jp)

Contents

Text S1: Methods

Hybrid back-projection method

The back-projection (BP) method estimates the spatiotemporal distribution of high-frequency radiation sources by time-shifting and stacking observed waveforms based on theoretical travel times and calculating signal intensity (Ishii et al., 2005; Krüger & Ohrnberger, 2005). However, reflected phases such as pP and sP can distort the timing of the estimated sources (Yagi et al., 2012). The hybrid back-projection (HBP) method (Yagi et al., 2012) calculates signal intensity by stacking cross-correlation functions of the observed waveforms and the Green's functions that include reflected phases, mitigating this problem and making it suitable for comparison with source-process models estimated by inversion (e.g., Okuwaki et al., 2014). For the HBP analysis, we used the same 47 stations as in the PDTI analysis and band-pass filtered the waveforms in two frequency bands: 0.3–1.0 Hz and 0.1–0.3 Hz. We then adopted *N*th root stacking ($N = 2$) (e.g., Muirhead and Datt, 1976). The HBP model surface followed the same nonplanar geometry used in the PDTI analysis. Knots were placed at intervals of 2 km in both the strike and dip directions. The theoretical Green's functions were calculated following the same procedure as in the PDTI analysis using the ak135-F model (Kennett et al., 1995; Montagner & Kennett, 1996).

Mach-cone analysis

In earthquakes involving supershear rupture, Rayleigh waves radiated from different locations along the source fault may arrive nearly simultaneously at stations located near the Mach cone. This compresses the apparent source duration within a narrow frequency band, causing the finite rupture to behave as an effective point source (Vallée & Dunham, 2012). At such stations, the Rayleigh-wave records of the mainshock are therefore expected to correlate strongly with those of a nearby smaller earthquake with a similar source location and focal mechanism, which is used as an empirical Green's function (EGF) event. This waveform similarity has been used in Mach-cone analyses to test for supershear rupture (e.g., Bao et al., 2019, 2022; Hicks et al., 2020; Xu et al., 2025; Zhang et al., 2022; Ren et al., 2024). In our analysis we used vertical-component broadband seismograms recorded on BHZ channels and retrieved through the FDSN web services. We used the M_W 6.4 earthquake (2009-09-12 20:06:25, 10.709°N, 67.927°W, 14.0 km depth) (U.S. Geological Survey, 2017) as the EGF event. The source location of the mainshock was set to the USGS-reported hypocenter of the M_W 7.2 event. We corrected the records for instrument response, converted them to displacement, and band-pass filtered them in the 10–25 s period range. Rayleigh-wave phase velocities were calculated using the GDM52 model (Ekström, 2011), and the predicted Mach-cone regions were determined for an assumed rupture velocity of 5 km/s (Figure S7). The waveform similarity of a pair of records at each station was evaluated using cross-correlation and the amplitude ratio (e.g., Bao et al., 2022).

Table S1: The structure model based on the CRUST1.0 (Laske et al., 2013) cell 1 (center: 10.5°N, 68.5°W)

V_P (km/s)	V_S (km/s)	Density (10^3 kg/m^3)	Thickness (km)
6.100	3.530	2.740	9.780
6.500	3.710	2.830	8.570
6.900	3.930	2.920	7.620
7.970	4.430	3.290	- (Moho)

Table S2: The structure model based on the CRUST1.0 cell 2 (center: 10.5°N, 67.5°W)

V_P (km/s)	V_S (km/s)	Density (10^3 kg/m^3)	Thickness (km)
6.100	3.530	2.740	9.710
6.500	3.710	2.830	9.410
6.900	3.930	2.920	8.370
7.940	4.420	3.280	- (Moho)

Table S3: The structure model based on the CRUST1.0 cell 3 (center: 10.5°N, 66.5°W)

V_P (km/s)	V_S (km/s)	Density (10^3 kg/m^3)	Thickness (km)
6.100	3.530	2.740	10.200
6.500	3.710	2.830	10.610
6.900	3.930	2.920	9.430
7.910	4.400	3.260	- (Moho)

Table S4: The structure model based on the CRUST1.0 cell 4 (center: 11.5°N, 68.5°W)

V_P (km/s)	V_S (km/s)	Density (10^3 kg/m^3)	Thickness (km)
1.500	0.000	1.020	0.250
6.000	3.500	2.720	8.780
6.600	3.800	2.860	6.550
7.100	3.900	3.050	10.910
8.060	4.480	3.320	- (Moho)

Table S5: The structure model based on the CRUST1.0 cell 5 (center: 11.5°N, 67.5°W)

V_P (km/s)	V_S (km/s)	Density (10^3 kg/m^3)	Thickness (km)
1.500	0.000	1.020	0.250
5.000	2.700	2.550	6.300
6.500	3.700	2.850	2.940
7.100	4.050	3.050	9.070
8.040	4.470	3.310	- (Moho)

Table S6: The structure model based on the CRUST1.0 cell 6 (center: 11.5°N, 66.5°W)

V_P (km/s)	V_S (km/s)	Density (10^3 kg/m^3)	Thickness (km)
1.500	0.000	1.020	0.250
6.000	3.500	2.720	6.110
6.600	3.800	2.860	3.810
7.100	3.900	3.050	6.340
7.980	4.440	3.290	- (Moho)

Table S7: The structure model based on the ak135-F model (Kennett et al., 1995; Montagner & Kennett, 1996)

V_P (km/s)	V_S (km/s)	Density (10^3 kg/m^3)	Thickness (km)
5.800	3.460	2.449	20.000
6.500	3.850	2.714	15.000
8.040	4.480	3.298	- (Moho)

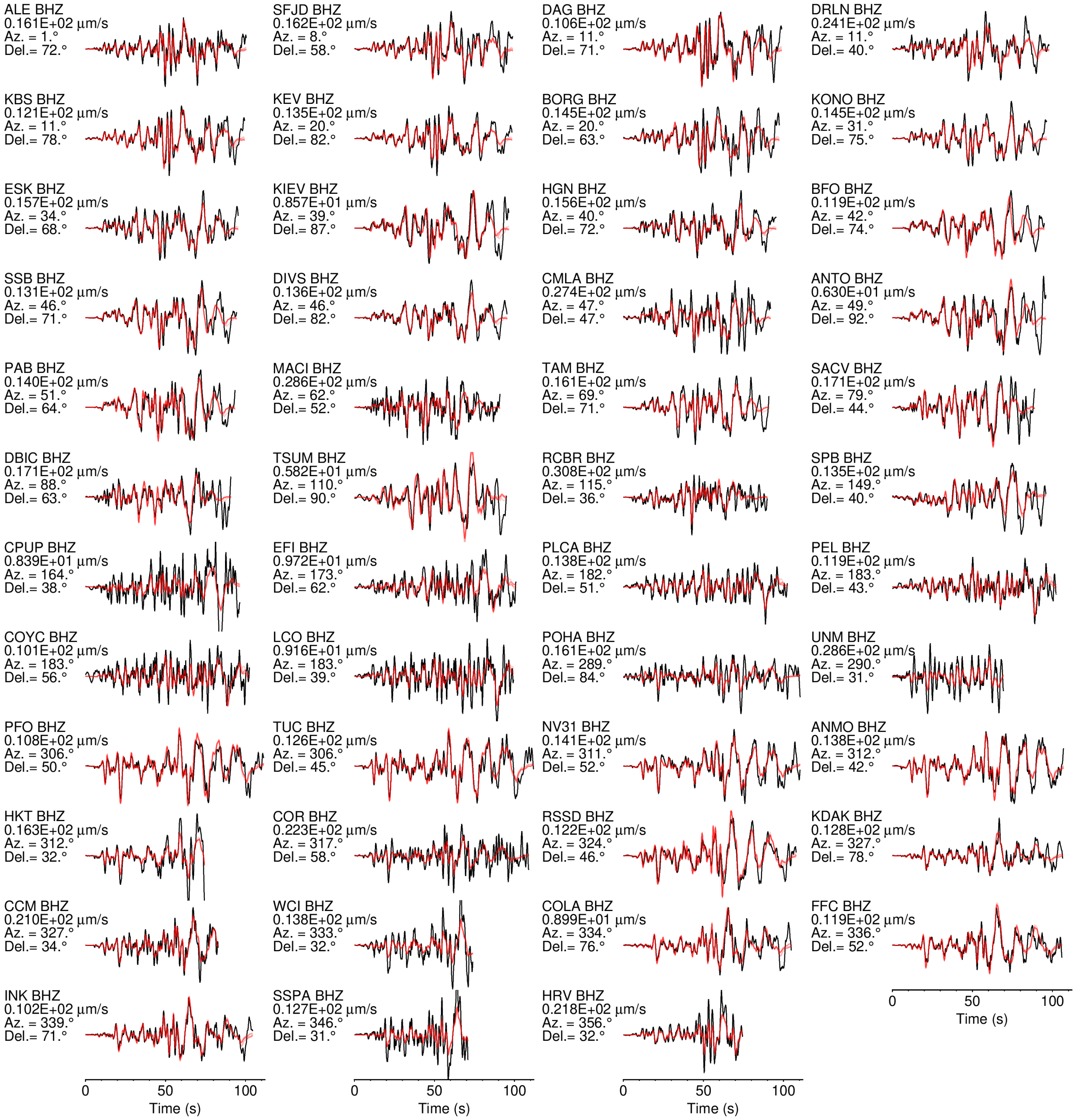

Figure S1

Comparison of observed waveforms (black) with synthetic waveforms of seven models (semi-transparent red). Each panel is labeled with the station code, maximum amplitude, azimuth (Az), and epicentral distance (Del). These waveforms were resampled to 20 Hz for plotting purposes.

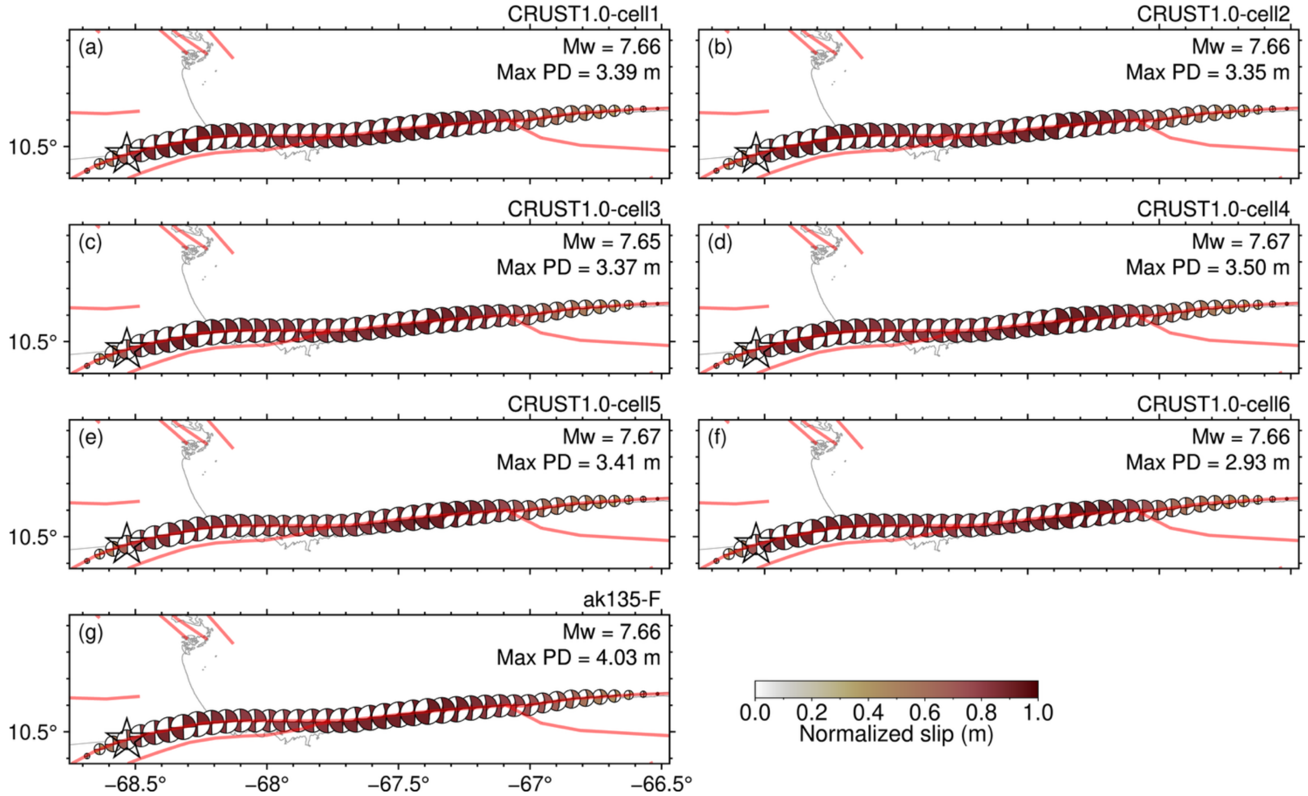

Figure S2

Map projection of potency density tensor distributions for seven models. (a-g) The focal mechanisms are plotted in order of slip, with those associated with larger slip plotted on top. The upper-right label in each panel indicates the model configuration (near-source structure model, moment magnitude, and maximum potency density). The maximum potency density for each model matches the upper limit of the normalized color scale. The red lines indicate active faults (Styron & Pagani, 2020).

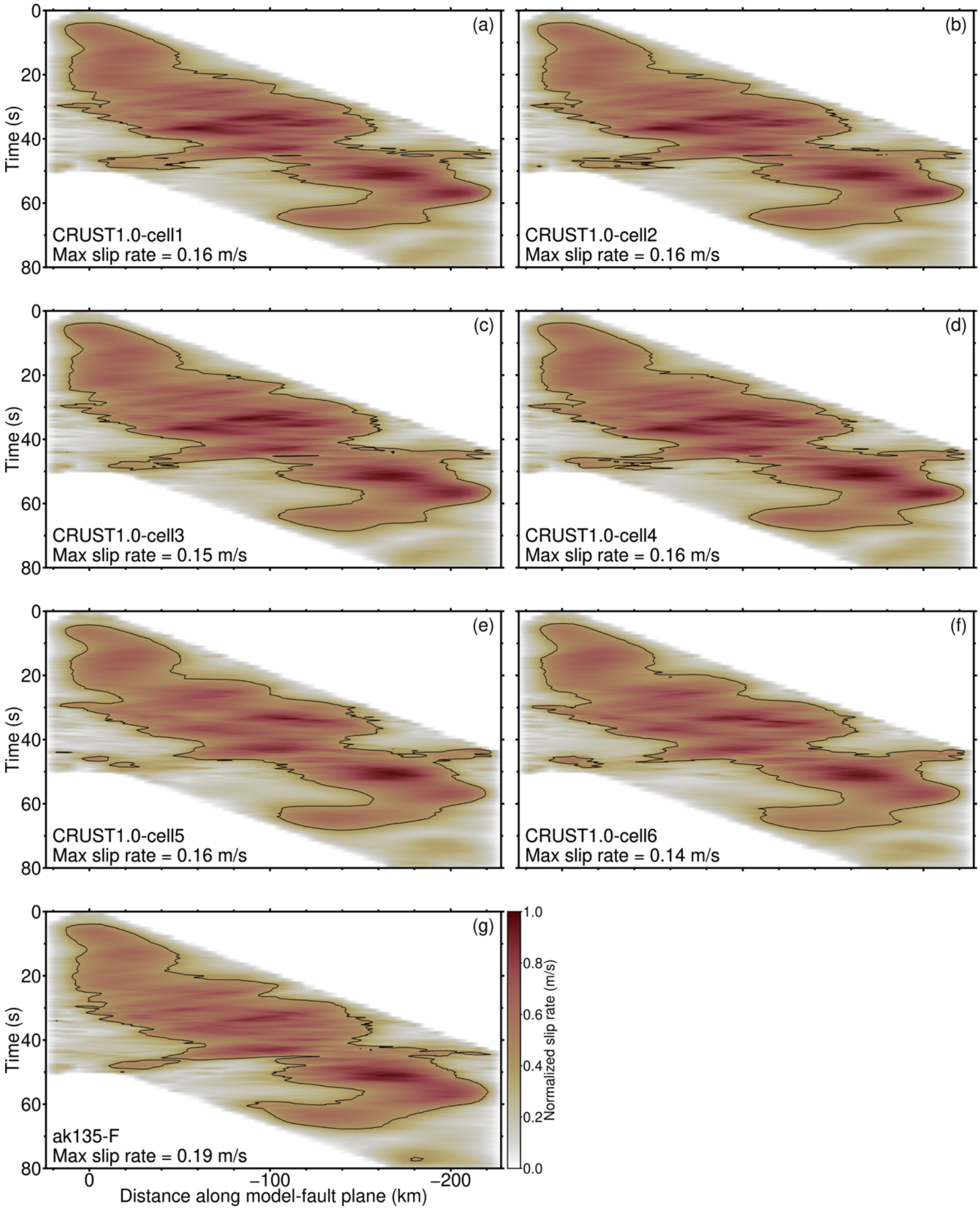

Figure S3

Spatiotemporal distributions of slip rate for seven models. (a-g) The horizontal axis denotes the along-strike distance from the hypocenter. The lower-left label in each panel indicates the model configuration (near-source structure model and maximum value of slip rate). The maximum slip rate for each panel matches the upper limit of the normalized color scale. The black lines indicate the 40% contours of the maximum slip rate.

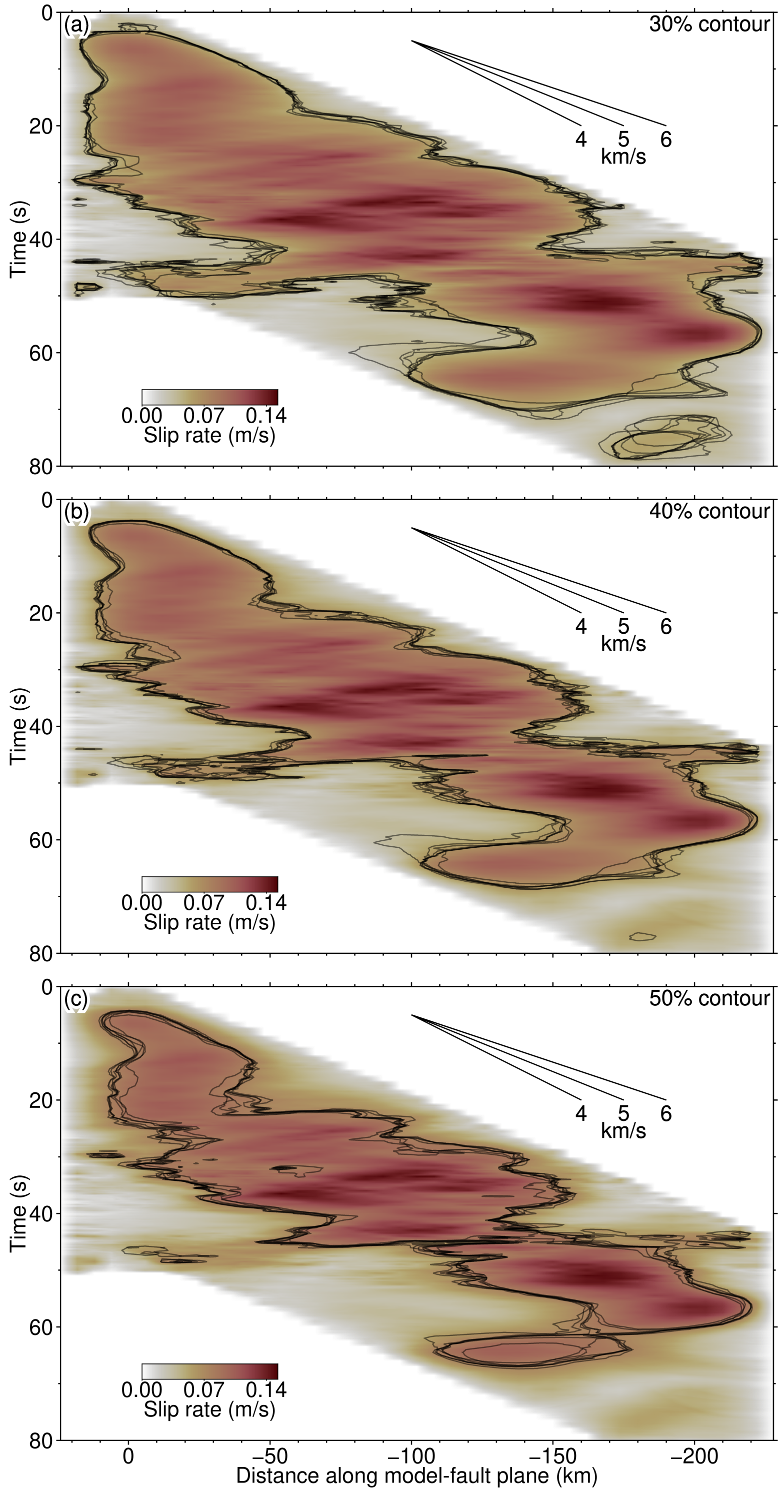

Figure S4

Spatiotemporal distributions of slip rate for contours set at (a) 30%, (b) 40%, and (c) 50% of the maximum slip rate for each of the seven models, projected with the strike direction of the model plane as the horizontal axis.

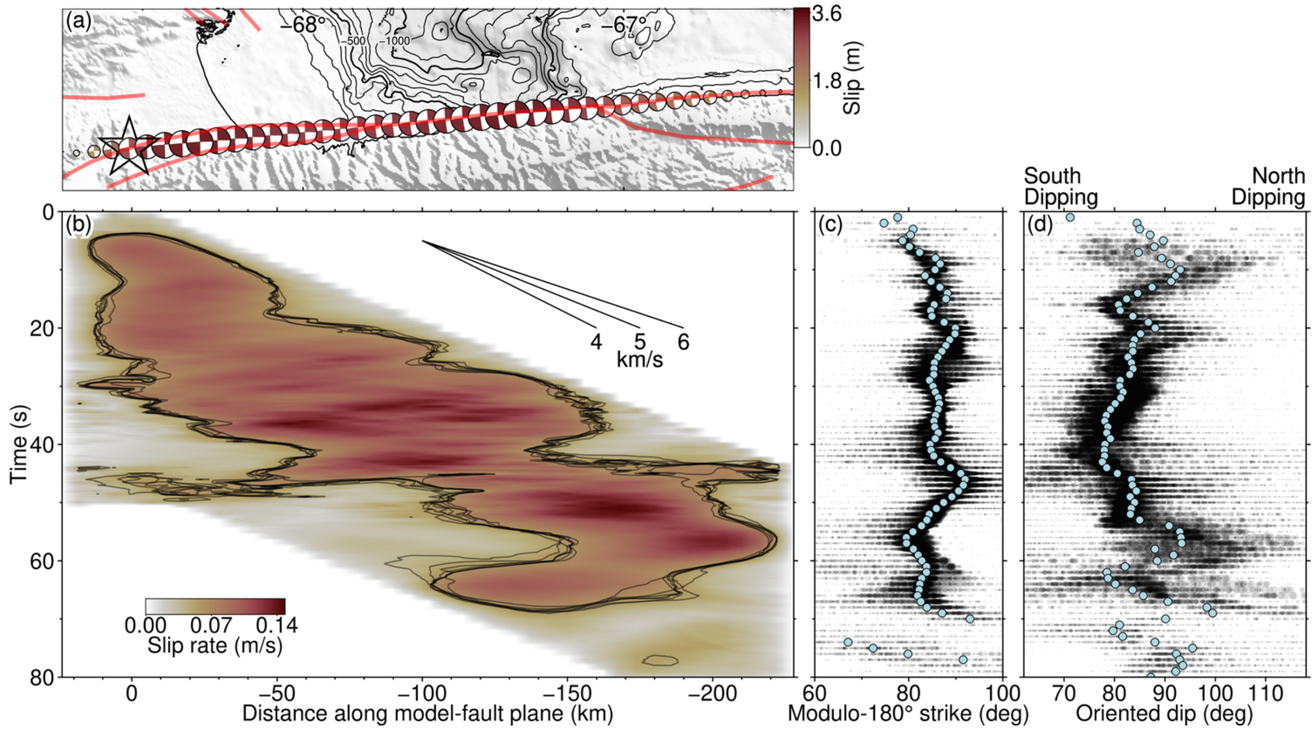

Figure S5

Overview of results using a planar fault model. The same seven structure models as those used in the analysis with the nonplanar model were used to calculate the Green's functions. (a) Map projection of the median distribution of the slip and the focal mechanisms calculated from the seven models. The focal mechanisms associated with larger slip are plotted on top. The star indicates the rupture initiation point defined based on the origin of the M_W 7.2 event reported by the USGS and FUNVISIS. The red lines indicate active faults (Alvarado et al., 2017; Audemard et al., 2000; Styron & Pagani, 2020). (b) Spatiotemporal distribution of the median slip rate projected with the strike direction of the model plane as the horizontal axis. The black lines indicate the 40% contours of the maximum slip rate for each of the seven models. (c) The temporal variation of the modulo-180° strike. (d) The temporal variation of the oriented dip. In (c) and (d), the blue dots represent the median value.

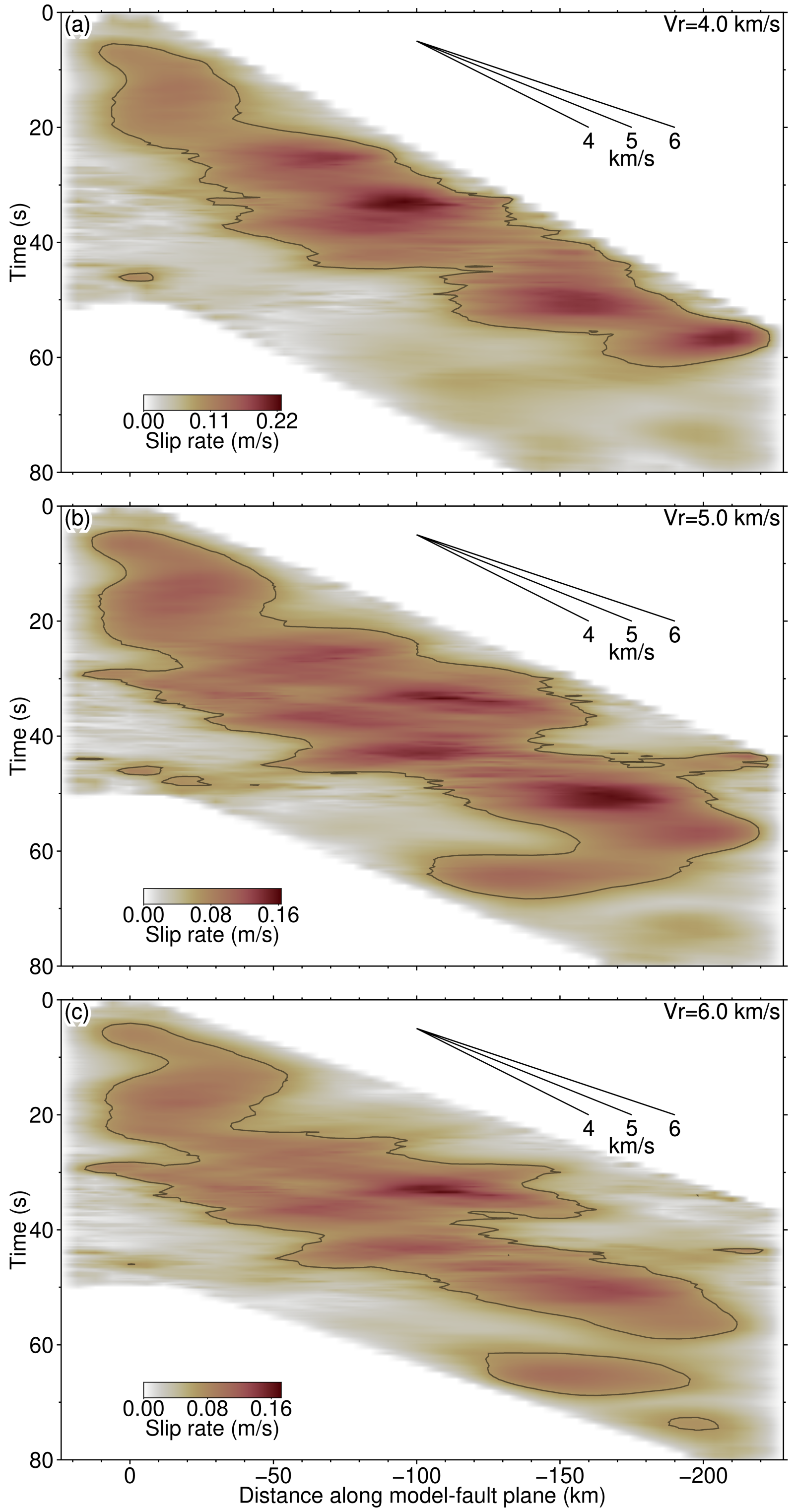

Figure S6

Spatiotemporal distributions of slip rate for inversions with the model-space boundary velocity, V_r, set to (a) 4 km/s, (b) 5 km/s, and (c) 6 km/s. The black lines indicate the 40% contours of the maximum slip rate over the complete spatiotemporal distribution of each model. The CRUST1.0 cell 5 structure model (Table S5) was used to calculate the Green's functions.

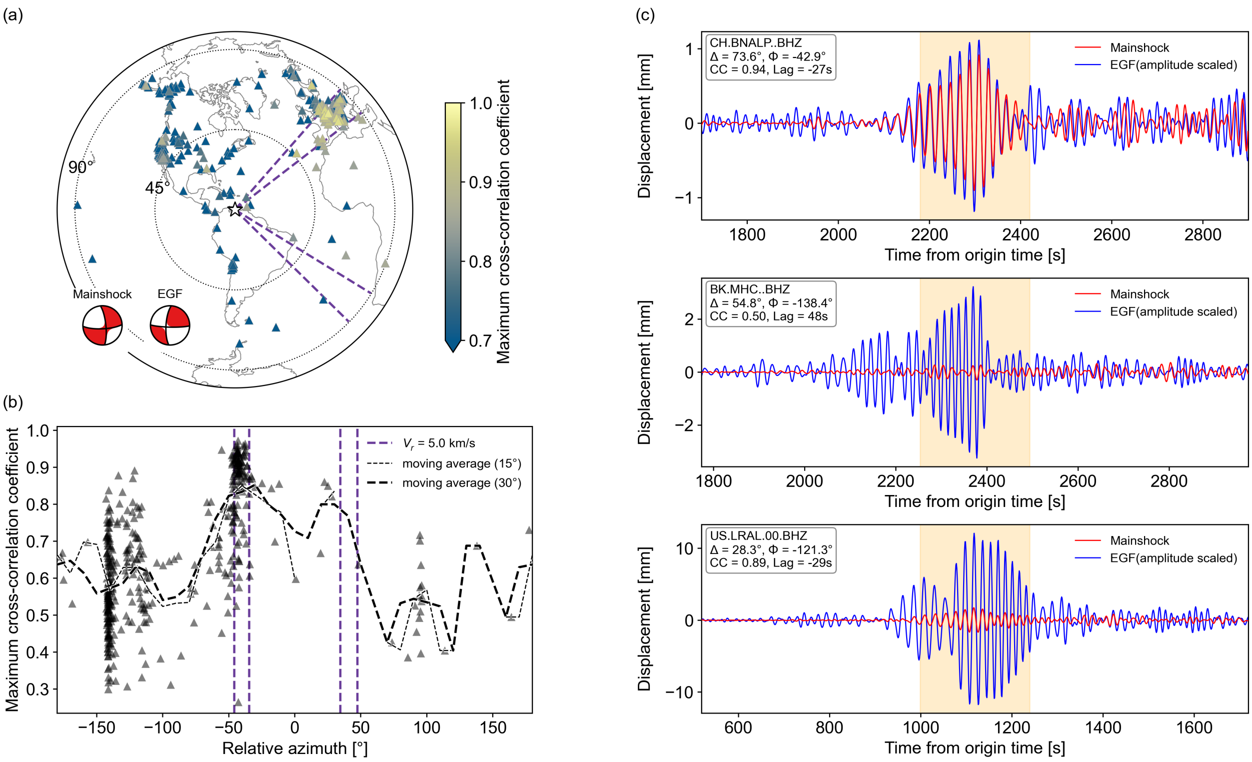

Figure S7

Mach-cone analysis for the 2026 Venezuela earthquake. (a) Map view of the result. The triangles indicate the stations, and the colors represent the values of the maximum cross-correlation (CC). The dashed lines indicate the Mach-cone area assuming a rupture-propagation velocity of 5 km/s. The two beachballs at the lower left show the GCMT solutions of the 2026 event (labeled as mainshock) and the EGF event (Dziewonski et al., 1981; Ekström et al., 2012). (b) Maximum CC at each station plotted against the azimuth relative to the rupture direction of 87°. The thin and thick dashed lines indicate moving averages of the maximum CC calculated using azimuthal windows of 15° and 30°, respectively. (c) The selected displacement records. The amplitude of the EGF-event waveform is scaled by the ratio of the seismic moment of the 2026 event to that of the EGF event. The yellow shading indicates the window used to calculate the cross-correlation. The trace ID is shown in the upper left, together with the epicentral distance (Δ), relative azimuth (Φ), maximum cross-correlation coefficient (CC), and the corresponding time lag (Lag). The time lag is used for aligning the EGF record. The top panel is for the station in the predicted Mach cones; the middle and bottom panels are for the stations outside the Mach cones. The bottom panel shows the highly similar records in phase, but the scaled amplitude of the EGF record does not match the mainshock record.